RSC Advances

PAPER

View Article Online
View Journal | View Issue

Cite this: *RSC Adv.*, 2020, **10**, 40005

An organic–inorganic hybrid nanomaterial composed of a Dowson-type $(NH_4)_6P_2Mo_{18}O_{62}$ heteropolyanion and a metal–organic framework: synthesis, characterization, and application as an effective adsorbent for the removal of organic dyes†

Akram-Alsadat Hoseini, Saeed Farhadi,* Abedin Zabardasti and Firouzeh Siadatnasab

In this work, an inorganic–organic hybrid nanomaterial, P_2Mo_{18}/MIL-101(Cr), based on Wells–Dawson-type $(NH_4)_6P_2Mo_{18}O_{62}$ polyoxometalate (abbreviated as P_2Mo_{18}) and the MIL-101(Cr) metal–organic framework was fabricated by the reaction of $(NH_4)_6P_2Mo_{18}O_{62}$, $Cr(NO_3)_3{\cdot}9H_2O$ and terephthalic acid under hydrothermal conditions. The as-prepared recyclable nanohybrid was fully characterized using X-ray diffraction (XRD), Fourier-transform infrared spectroscopy (FT-IR) equipped with energy dispersive X-ray microanalysis (EDX), field emission scanning electron microscopy (FE-SEM), Raman spectroscopy and Brunauer–Emmett–Teller (BET) specific surface area studies. All the analyses confirmed the successful insertion of $P_2Mo_{18}O_{62}^{6-}$ heteropolyanion within the cavities of MIL-101(Cr). The encapsulated MIL-101(Cr) showed a considerable decrease in both pore volume and surface area compared with MIL-101(Cr) due to incorporation of the very large Dowson-type polyoxometalate into the three-dimensional porous MIL-101(Cr). The nanohybrid had a specific surface area of 800.42 $m^2\ g^{-1}$. The adsorption efficiency of this nanohybrid for removal of methylene blue (MB), rhodamine B (RhB), and methyl orange (MO) from aqueous solutions was evaluated. Surprisingly, the composite not only presented a high adsorption capacity of 312.5 mg g^{-1} for MB, but also has the ability to rapidly remove 100% MB from a dye solution of 50 mg L^{-1} within 3 min. These results confirmed that this adsorbent is applicable in a wide pH range of 2–10. The nanohybrid showed rapid and selective adsorption for cationic MB and RhB dyes from MB/MO, MB/RhB, MO/RhB and MB/MO/RhB mixed dye solutions. The equilibrium adsorption data were better fitted by the Langmuir isotherm. Kinetics data indicate that the adsorption of the dye follows a pseudo-second order kinetics model. Also, this material could be effortlessly separated and recycled without any structural modification. Accordingly, it is an efficient adsorbent for removing cationic dyes.

Received 15th August 2020
Accepted 18th October 2020

DOI: 10.1039/d0ra07042d

rsc.li/rsc-advances

1. Introduction

Pollution of water with organic compounds is a challenging environmental issue in many countries.[1,2] Predominantly, organic dyes are comprehensively used in the industries of silk, cosmetics, cotton, linen, wool, plastics, textiles and leather, printing paper, *etc.*[3–6] The removal of these pollutants from contaminated aqueous solutions is of great importance in environmental processes.[7] At present, different treatment technologies, including biological methods, chemical oxidation, ion exchange, organic treatment, adsorption, membrane technologies and photocatalytic or sonocatalytic degradation, are being created and utilized in the expulsion of dyes.[8–13] Among the existing elimination procedures, adsorption methods are the most practical for deletion of pigments and organic dyes from aquatic media on a large scale with a suitable choice of adsorbent, as these approaches can yield high-quality water using economically viable processes.[14] Many forms of materials are employed as adsorbents for water decontamination, such as zeolites, clays, activated carbons, graphene oxide and polymeric materials. On the other hand, some of these materials are only effective for wastewater with low concentrations of dye, and they normally show very poor performance in

Department of Chemistry, Lorestan University, Khorramabad 68151-433, Iran. E-mail: farhadi.s@lu.ac.ir; Fax: +98 66 33120618; Tel: +98 66 33120611

† Electronic supplementary information (ESI) available. See DOI: 10.1039/d0ra07042d

selectively removing targeted organic dyes. The goal is to discover an appropriate adsorption material which not only has the ability to reduce pollutant organic dyes with low loss and high efficiency, but also enables selective separation and recovery of raw materials.[15,16]

Polyoxometalates (POMs) are an exceptional family of metal oxide clusters with manageable shapes and sizes, rich redox reactions, high electronegativity, oxo-enriched surfaces, rich topologies and photoactivity; they have been used in many exploration fields, including biochemistry, chemical analysis, sensors, catalysis, ion-selective membranes, magnetism and proton exchange membranes.[17] However, the submission of pure POMs as adsorbents or catalysts is imperfect because of their comparatively low surface areas (5–8 $m^2\ g^{-1}$), the according seriously obstructed accessibility to their active sites, and their high dissolvability in water, which creates difficulty in detaching them from the reaction mixture.[18] To overcome these problems, the immobilization of POMs on solid supports to build hybrid materials has been attempted. In this circumstance, materials such as titania, zirconia, activated carbon, silica, Fe_2O_3, graphene, Al_2O_3, UiO-66 and MOFs have been employed for synthesis of hybrid materials with POMs.[8,19–22] In this work, to address these limitations, metal–organic frameworks (MOFs) have been considered for anchoring of POMs to form hybrid heterogeneous materials.

Metal–organic frameworks (MOFs) are coordination polymers which are self-assembled from polydentate organic ligands and transition metal cations; they are attracting growing attention in the fields of gas separation and storage, catalysis, luminescence, elimination and adsorption of organic pollutants due to their crystalline natures, ultrahigh porosities, ultrahigh surface areas and tunable pore sizes.[23–32] Among the MOFs that are known to date, MIL-101 is a well-recognized robust MOF that possesses two hydrophilic zeotypic cavities with pore sizes of 29 Å and 34 Å and an exceedingly high specific surface area (SBET $\approx$ 4000 $m^2\ g^{-1}$). Principally, due to the fundamentally greater porosities and extraordinarily large BET surface areas of MOFs, they have become attractive host matrices for the encapsulation of POMs.[33,34] Therefore, MIL-101(Cr) can be used as a reference MOF for investigating various guest–host interactions for aqueous organic pollutant removal. In the last two decades, a chain of hybrid materials constructed with the MIL-101 MOF and various POMs have been described and studied in various application fields, such as organic reactions, electrocatalytic reactions, photocatalytic reactions and dye adsorption.[35,36]

In this work, the P_2Mo_{18}/MIL-101(Cr) nanohybrid was fabricated for the first time by a hydrothermal technique. This POM/MOF inorganic–organic nanohybrid material was fully characterized. The adsorption of RhB, MO, and MB organic dyes by P_2Mo_{18}/MIL-101(Cr) and the effects of contact time, adsorbent dosage, pH, initial dye concentration and solution on the adsorption trend were investigated. As additional features, the isotherms and kinetics of the adsorption of MB onto the compound were studied. Also, the recyclability and stability of the nanohybrid were carefully explored. The fabricated hybrid nanomaterial revealed selective adsorption abilities with superior adsorption rates for MB and RhB cationic dyes compared to the MIL-101 framework alone.

2. Experimental

2.1. Materials

Terephthalic acid (H_2BDC, 98%), chromium(III) nitrate ($Cr(NO_3)_3\cdot 9H_2O$, 99%), sodium tungstate ($Na_2MoO_4\cdot 2H_2O$, 99%), phosphoric acid (H_3PO_4, 85%), hydrochloric acid (HCl, 35%), ammonium chloride (NH_4Cl, 99%), methanol and ethanol were obtained from Merck, as were the organic dyes methylene blue (MB), rhodamine B (RhB) and methyl orange (MO), which were of the highest available purity.

2.2. Fabrication of $(NH_4)_6P_2Mo_{18}O_{62}$ (P_2Mo_{18})

$(NH_4)_6P_2Mo_{18}O_{62}$ was prepared according to a literature method with some modifications.[37] Briefly, a mixture of $Na_2MoO_4\cdot 2H_2O$ (85.12 g), concentrated H_3PO_4 (15 mL) and HCl (80 mL) in distilled water (450 mL) was refluxed for 8 h. After cooling, 100 g NH_4Cl was added. A green precipitate was perceived instantly after the addition of ammonium chloride. The resulting suspension was maintained overnight at 5 °C in order to enhance the precipitation. The product was filtered through a Buchner funnel and re-dissolved in an equal weight of distilled water. This solution was filtered to separate dissolved impurities. To obtain a perfectly clear solution, solid NH_4Cl was added to make a 20 wt% solution. After 8 h, the crystals were filtered and re-dissolved in the minimum amount of distilled water. The resulting solution was vaporized in a rotary evaporator (40 °C) under low pressure. Finally, the precipitate was filtered off and washed with anhydrous diethyl ether and ethanol.

2.3. Fabrication of the P_2Mo_{18}/MIL-101(Cr) adsorbent

In a distinctive one-pot fabrication, deionized water (30 mL) with a mixture of Cr $(NO_3)_3\cdot 9H_2O$ (2.0 g, 5 m mol), H_2BDC (0.83 g, 5 m mol), and $(NH_4)_6P_2Mo_{18}O_{62}$ (2.0 g, 0.7 m mol) was dispersed under 10 min of sonicating. The mixture was moved to a 50 mL Teflon-lined autoclave and heated at 200 °C for 24 h under hydrothermal conditions. Then, the mixture was gently cooled to room temperature. The resulting precipitate was filtered, washed with deionized water and ethanol, and dried at room temperature. The ICP-AES results indicated that the loading amount of P_2Mo_{18} in the as-prepared P_2Mo_{18}/MIL-101(Cr) nanocomposite was estimated to be 36.85 wt%. For comparison, pure MIL-101(Cr) sample was also prepared under the same conditions without adding P_2Mo_{18}.

2.4. Characterization methods

FTIR spectra were obtained with a Shimadzu-8400S (Japan) spectrometer in the wavenumber range of 400–4000 cm^{-1}; an X-ray diffractometer (Philips X-Pert 8440) with Cr Kα radiation ($\lambda = 2.289$ Å) was employed for X-ray diffraction (XRD) analysis of the powder samples. The shapes and morphologies of the samples were perceived by a MIRA3 TESCAN field emission scanning electron microscope (FESEM) armed with a link

energy-dispersive X-ray (EDX) analyzer. BET measurements were performed to determine the specific surface areas and porosities of the samples with N_2 adsorption measurements at 77 K using a BELSORP Mini instrument. The samples were degassed at 180 °C prior to the nitrogen adsorption measurements. An adsorption isotherm was considered to determine the pore size distribution by the Barrett–Joyner–Halenda (BJH) method. A Raman microscope (Senterra 2009, Germany) equipped with a laser wavelength of 758 nm was employed to obtain the Raman spectra. The adsorption mechanisms of the dyes were investigated at room temperature on a Varian Cary 100 spectrophotometer. The content of P_2Mo_{18} in the nanocomposite was determined by inductively coupled plasma atomic emission spectroscopy (ICP-AES, model OEC-730).

2.5. Dye adsorption tests

To investigate the properties of the nanohybrid, adsorption experiments were executed in 100 mL glass pyramic bottles, and the adsorption reaction temperature was maintained at 25 °C. Freshly fabricated nanohybrid (30 mg) was placed in 50 mL of aqueous solutions of different colorants, including rhodamine B (RhB), methylene blue (MB) and methyl orange (MO), with initial concentration sof 50 mg L^{-1}. At scheduled time intervals, a small portion (2 mL) of the solution was pipetted out and centrifuged at 5000 rpm for 5 min to separate the solid adsorbent portion. The residual amounts of dyes were determined at 664, 553 and 467 nm for MB, RhB and MO, respectively, with a spectrophotometer.

The effects of solution pH (2–10), adsorbent dosage (10, 20 and 30 mg), and initial MB concentration (50–200 mg L^{-1}) on the adsorption performance of the as-prepared adsorbent were studied under similar conditions. Also, the nanohybrid was poured into mixtures of MO/RhB, RhB/MB, MO/MB (v/v 1/1, 50 mL, 50 mg L^{-1}) and MB/RhB/MO (v/v 1/1/1, 50 mL, 50 mg L^{-1}) to study the adsorption selectivity activity of the adsorbent.

The adsorption capacity (q_e) (mg g^{-1}) and elimination rate (R%) were calculated based on the following eqn (1) and (2):

$$q_e = [(C_0 - C_{eq})/m] \times V \quad (1)$$

$$R = [(C_0 - C_t)/C_0] \times 100 \quad (2)$$

where C_0 and C_t (mg L^{-1}) are the initial dye concentration and the dye concentration at time (t), respectively, V is the volume of the dye solution (mL), and m is the amount of adsorbent (mg).

3. Results and discussion

In this work, a nanohybrid material, P_2Mo_{18}/MIL-101(Cr), was prepared by the reaction of the ammonium salt of the Dowson-type polyoxomolybdate $(NH_4)_6P_2Mo_{18}O_{62}$ (abbreviated as P_2Mo_{18}) with the MIL-101(Cr) MOF in aqueous solution under hydrothermal conditions at 200 °C for 24 h. During the formation of the MIL-101(Cr) framework, P_2Mo_{18} polyanions could be trapped in the holes of the MOF, resulting in the P_2Mo_{18}/MIL-101(Cr) nanohybrid. From the ICP-AES results, the loading amount of P_2Mo_{18} in the as-prepared P_2Mo_{18}/MIL-101(Cr) hybrid was estimated to be 36.85 wt%. The preparation process of this inorganic–organic hybrid nanomaterial is illustrated in Scheme 1. The structure and composition of the hybrid nanomaterial were further characterized by FT-IR, Raman spectroscopy, XRD, SEM, EDX, and BET surface area analyses.

3.1. FT-IR analysis

To confirm the presence of P_2Mo_{18} within the pores and the structure of MIL-101(Cr), the composite P_2Mo_{18}/MIL-101(Cr) was characterized by FT-IR spectroscopy. The FT-IR spectra of the P_2Mo_{18}, MIL-101(Cr) and P_2Mo_{18}/MIL-101(Cr) samples are shown in Fig. 1. As shown in Fig. 1(a), the characteristic bands of Dawson heteropolyanion are observed at 1076 (the stretching

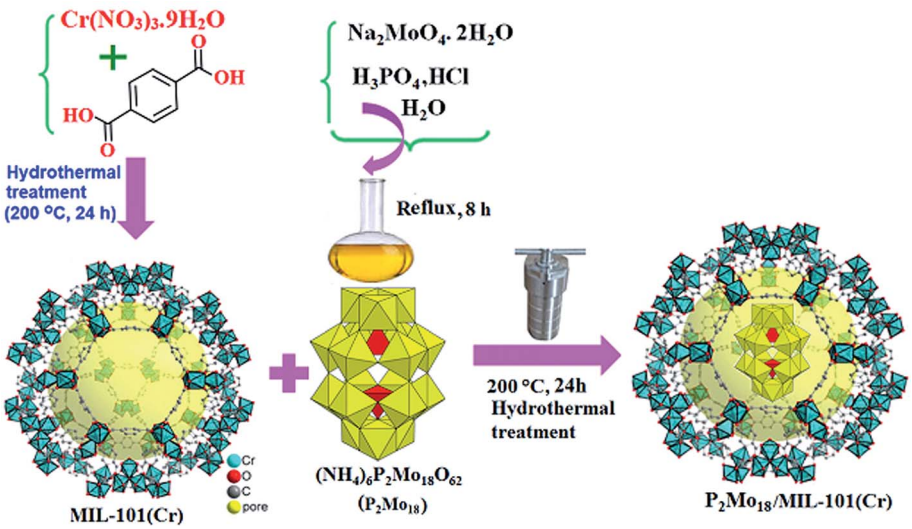

Scheme 1 The preparation process of the P_2Mo_{18}/MIL-101(Cr) inorganic–organic hybrid nanomaterial.

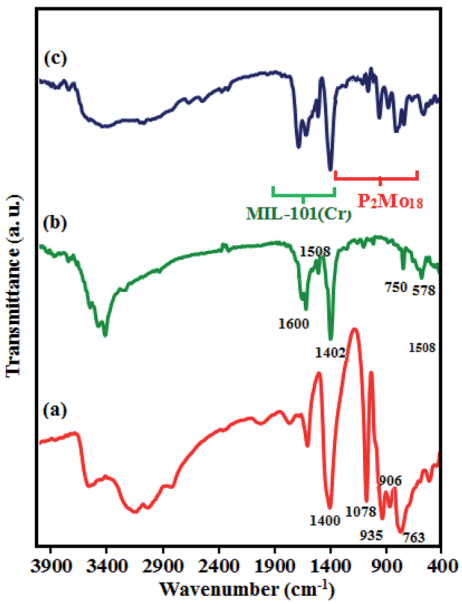

Fig. 1 The FT-IR spectra of (a) MIL-101(Cr), (b) P_2Mo_{18}, and (c) P_2Mo_{18}/MIL-101(Cr).

frequency of the P–O bonds of the PO_4 units), 935 (Mo=O terminal bands), and 906 and 763 cm^{-1} (Mo–O–Mo "inter" and "intra" Mo–O–Mo bridges), respectively.[38] Our salt also exhibited the infrared signal of the NH^{4+} species at 1400 cm^{-1}.[39] The FT-IR spectrum of MIL-101(Cr) in Fig. 1(b) shows two sharp peaks at 1600 and 1402 cm^{-1}, which are allotted to asymmetric and symmetric vibrations of the carboxyl groups (O–C–O) in H_2BDC, respectively, endorsing the presence of the dicarboxylate linker in the fabricated sample.[40] The additional bands between 600 and 1600 cm^{-1} were attributed to benzene, including the stretching vibration (C=C) at 1508 cm^{-1} and the deformation vibration (C–H) at 750 cm^{-1}, whereas the peak detected at 578 cm^{-1} is associated with the symmetric stretching of Cr–O.[41,42] After forming the $P_2Mo_{18}O_{62}$/MIL-101(Cr) nanocomposite, as publicized in Fig. 1(c), the characteristic peaks related to MIL-101(Cr) and P_2Mo_{18} slightly shifted. These shifts suggest an interaction between the P_2Mo_{18} anion and MIL-101(Cr) MOF.

3.2. Raman spectroscopy

The presence of the Dawson-type polyoxomolybdate (P_2Mo_{18}) in the MIL-101(Cr) framework was further confirmed by the Raman spectrum of the fabricated nanohybrid in comparison with those of the compounds alone, as shown in Fig. 2(a–c). As can be perceived in Fig. 2, the Raman spectrum of the P_2Mo_{18}/MIL-101(Cr) nanocomposite shows the typical bands of the porous support material MIL-101 as well as, more or less, the vibrational modes of P_2Mo_{18}. In particular, the signals at 979 and 715 cm^{-1}, accredited to the stretching mode of the terminal Mo–Od and to the Mo–O–Mo stretching mode, respectively, ae apparent in the spectrum of P_2Mo_{18}/MIL-101(Cr).[42,43] The characteristic bands validate the existence of both P_2Mo_{18} and MIL-101 in the P_2Mo_{18}/MIL-101(Cr) nanohybrid.

3.3. X-ray powder diffraction (XRD)

The crystal structures and phase compositions of the samples MIL-101(Cr), P_2Mo_{18}, and P_2Mo_{18}/MIL-101(Cr) were characterized by XRD, and the results are shown in Fig. 3(a–c). With respect to collected works, Fig. 3(a) evidently shows the normal

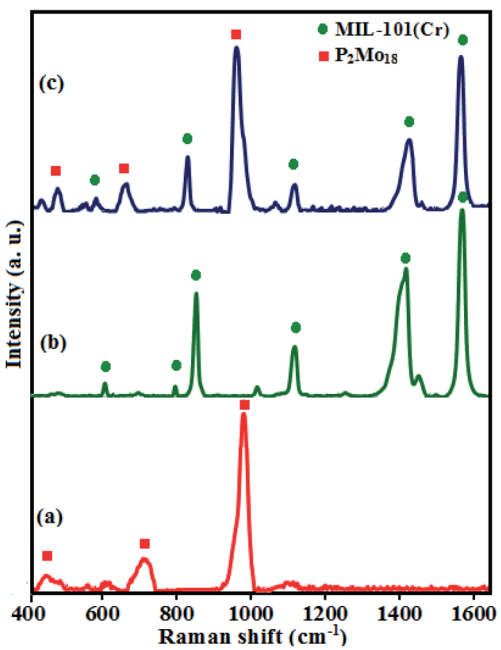

Fig. 2 FT-Raman spectra of (a) P_2Mo_{18}, (b) MIL-101(Cr) and (c) P_2Mo_{18}/MIL-101(Cr).

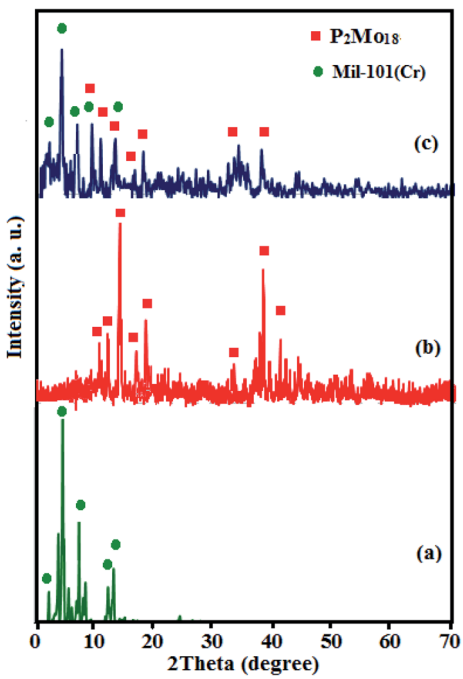

Fig. 3 XRD patterns of (a) MIL-101(Cr), (b) P_2Mo_{18}, and (c) P_2Mo_{18}/MIL-101(Cr).

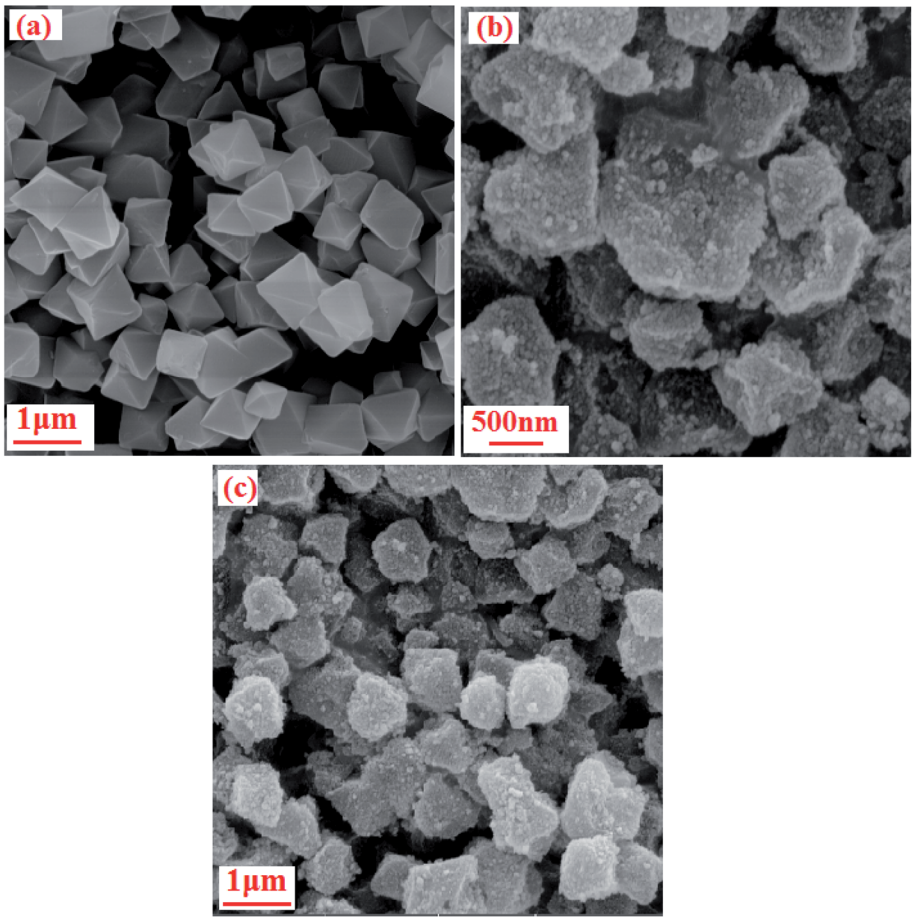

Fig. 4 FE-SEM images of (a) MIL-101(Cr) and (b and c) the P_2Mo_{18}/MIL-101(Cr) nanocomposite.

characterization peaks of MIL-101(Cr) at 2θ 2.9°, 3.4°, 5.2°, 8.5°, 9°, and 12.3° at high intensity, which indicates the high crystallinity of the obtained MIL-101(Cr).[44,45] As indicated in Fig. 3(c), all of the diffraction peaks corresponding to both P_2Mo_{18} and MIL-101(Cr) and no other impurity peaks can be witnessed. Only the widths and diffraction peak intensities demonstrate some changes, confirming that the framework of the MOF did not change in the course of the encapsulation process of P_2Mo_{18} into the cages of MIL-101(Cr).

3.4. SEM analysis

The morphology and size of the P_2Mo_{18}/MIL-101(Cr) nanohybrid were analyzed using FE-SEM observations, as shown in Fig. 4. In Fig. 4(a), the pure MIL-101(Cr) particles can be seen to possess a regular octahedral morphology with a rather narrow size distribution. The magnitudes of these octahedral crystals are in the sub-micrometer range (0.4–1.0 mm). The SEM photographs of the P_2Mo_{18}/MIL-101(Cr) composite in Fig. 4(b and c) validate that the shape and morphology of this sample are not the same as those of the pristine MIL-101(Cr). The SEM pictures of P_2Mo_{18}/MIL-101(Cr) do not demonstrate perfect polyhedral morphologies. Additionally, the Raman, XRD and FT-IR results testify that the framework of MIL-101(Cr) was not destroyed or broken down after incorporation of P_2Mo_{18} phase, although its morphology changed.

3.5. Energy dispersive spectroscopy (EDX)

Energy dispersive X-ray (EDX) analysis confirmed the composition of the as-fabricated nanohybrid. The presence of C, O, Cr, N, P and Mo elements in the P_2Mo_{18}/MIL-101(Cr) nanohybrid was confirmed by the EDX spectrum (Fig. 5). Fig. 5(a) displays a SEM image of the nanocomposite with the corresponding EDX elemental mappings. The elemental peaks attributed to C, O, Cr, N, P, and Mo in the existing EDX spectrum in Fig. 5(b) confirmed their presence in the P_2Mo_{18}/MIL-101(Cr) nanocomposite. It can be perceived in the maps that the C, O, Cr, N, P, and Mo elements are consistently distributed over the image, ratifying the homogeneity of the sample. The results of the EDX mappings confirm that the shape of the product was similar to that perceived using FE-SEM.

3.6. BET specific surface area analysis

N_2 adsorption/desorption measurements were performed to determine the BET surface areas and the pore size distributions of the samples. The nitrogen adsorption–desorption isotherms of MIL-101(Cr) and the P_2Mo_{18}/MIL-101(Cr) samples are

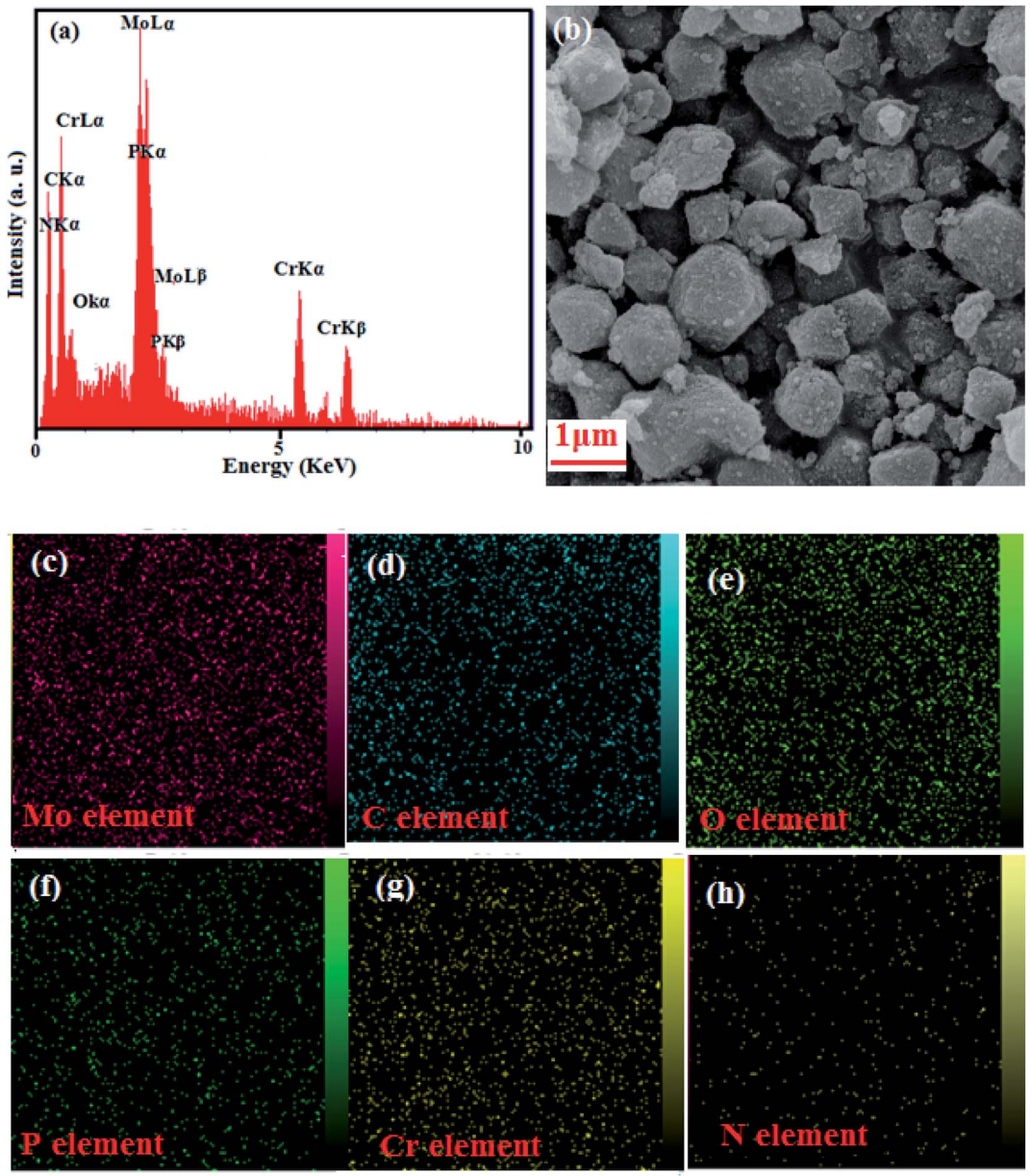

Fig. 5 (a) SEM spectrum and (b–h) representative EDX photographs of the P_2Mo_{18}/MIL-101(Cr) with corresponding EDX elemental mappings.

displayed in Fig. 6(a). They show type I isotherms with H_4-type hysteresis loops, according to the IUPAC classification, which are characteristic of solids with microporous windows and mesoporous cages.[46] Compared with the pristine MIL-101, significant decreases in the surface area, pore volume, and pore diameter of the encapsulated samples were observed owing to the insertion of POMs into the cavities of MIL-101, which occupied some of the pore space (Table 1). The Barrett–Joyner–Halenda (BJH) pore-size distributions in Fig. 6(b) also confirm that the average pore size of the composite is smaller than of MIL-101(Cr). Based on these results, the P_2Mo_{18} polyanion was encapsulated inside the channels of MIL-101(Cr) more than on the outer surfaces.

3.7. Adsorption properties

After successful innovative fabrication of the nanocomposite, its adsorptivity for removing colorants from polluted water was weighed through a typical procedure. Three organic dyes (MB, RhB and MO) with dissimilar sizes and charges were chosen for experimentation. The concentrations of MB, RhB and MO were considered from UV-Vis absorption studies by means of the Beer-Lambert law relation at maximum wavelengths (λ_{max}) of 664, 553 and 463 nm, respectively. As shown in Fig. 7, the bands decreased deliberately with adsorption time according to the reduction of the colorant concentration. For MB, the adsorption efficiency was 100% in 3 min, and that of RhB was about 99% in 15 min; however, that of MO was almost negligible. Therefore, the exceptional adsorption properties of the P_2Mo_{18}/

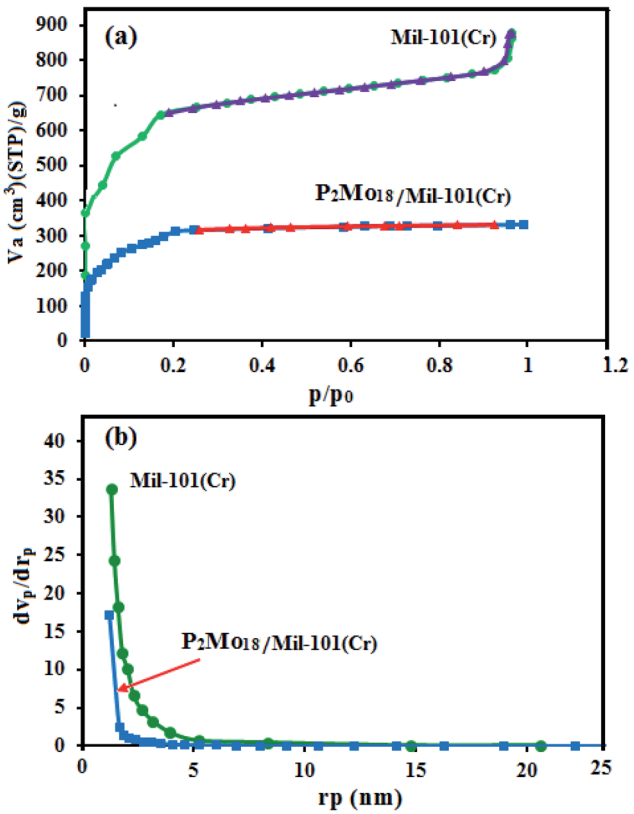

Fig. 6 (a) N_2 adsorption–desorption isotherms and (b) BJH pore-size distribution plots for the MIL-101(Cr) and P_2Mo_{18}/MIL-101(Cr) samples.

MIL-101(Cr) nanocomposite towards the cationic MB and RhB molecules were clearly demonstrated. The diverse effects on the removal of colorants can be linked to the structures of the dye molecules and of the nanocomposite as well. This is due to the presence of highly electronegative POM, which mostly enhanced the adsorption ability of the porous material MIL-101(Cr); together with the enormous numbers of negative charges, this may exert a stronger force on colorants with positive charges. The fabricated material in this study is not an efficient adsorbent for removal of MO because of the negative charges of both the adsorbent and dye molecules. As a consequence, neither electrostatic attraction nor adsorption occurs between the POM encapsulated into the nanocomposite and MO molecules.

3.7.1. Selective dye adsorption. One of the most attractive and challenging complications in the process of dye–wastewater treatment is selective adsorption and separation of specific dyes. To achieve this target, different mixtures of dye solutions with various sizes and charges were chosen for investigation, bearing in mind that the size and charge of an organic dye are the two major factors controlling the adsorption process. This property was tested by preparing mixtures of MB + MO, MB + RhB and MO + RhB (50 mL, $C_{0(MB)} = C_{0(RhB)} = C_{0(MO)} = 50$ mg L^{-1}) with 30 mg of P_2Mo_{18}/MIL-101(Cr) as the absorbent, followed by monitoring the processes by UV-visible spectroscopy. Based on Fig. 8(a) and (b), the superior removal of the cationic MB and RhB from the MB + MO and RhB + MO mixtures can be attributed to the anionic nature of P_2Mo_{18}/MIL-101(Cr). A binary mixture of cationic dyes (MB + RhB) was selected; the results in Fig. 8(c) reveal that both dyes adsorbed completely but that the complete adsorption of RhB needs a longer time due to its larger volume. For better judgment, the results of a ternary mixture of MB, RhB and MO in Fig. 8(d) show that MB was also adsorbed entirely in the initial 1 min and that complete adsorption of RhB requires a longer time of 10 min because of its greater molecular volume; meanwhile, the characteristic absorption peaks of MO were retained. These results confirm that the P_2Mo_{18}/MIL-101(Cr) nanohybrid is a worthy nominee for selective adsorption and separation of cationic dyes.

In Table 2, we also compare the above results for the removal of MB by the nanohybrid with some similar adsorbents in the literature. Accordingly, with respect to the adsorption time (which is shorter than that of most reported adsorbents), initial dye concentration and adsorption capacities, the current presented method is more advantageous, suitable and/or superior.

3.7.2. Influence of adsorbent dose. For the purpose of wastewater purification, determining a suitable adsorbent dosage is very important. The effects of the P_2Mo_{18}/MIL-101(Cr) dosage on the exclusion of MB were investigated with different adsorbent amounts of P_2Mo_{18}/MIL-101(Cr) (10.0, 20.0, and 30.0 mg) in 50 mL of dye solutions (50 mg L^{-1} at pH 6) (Fig. 9(a)). Accordingly, due to the more available vacant surface sites during the early stage of the process, the MB adsorption rises but is followed by a drop until a state of equilibrium is reached after 3 min for all samples. The removal percentages of MB for 10, 20 and 30 mg of adsorbent were calculated to be 45%, 91% and 100%, respectively, in 3 min. Finally, the optimized adsorbent dosage was found to be 30 mg.

3.7.3. Influence of initial pH. The adsorption removal capacity depends on the surface properties of the adsorbent and the structure of the adsorbate, which are greatly affected by pH. The measurements of the zeta potential and influence of the pH solution value on the adsorption of MB were investigated, and the results are illustrated in Fig. 9(b). At natural pH, the zeta potential measured for the P_2Mo_{18}/MIL-101(Cr) adsorbent is about −24.02 mV (see Fig. S1†). This value indicates that the P_2Mo_{18}/MIL-101(Cr) surface is negatively charged. The MB

Table 1 The texture parameters of MIL-101(Cr) and the P_2Mo_{18}/MIL-101(Cr) nanocomposite

Entry	Sample	BET surface area (m^2 g^{-1})	Langmuir surface area (m^2 g^{-1})	Total pore volume (cm^3 g^{-1})	Average pore diameter (nm)
1	MIL-101(Cr)	2452.50	3279.50	0.532	1.30
2	P_2Mo_{18}/MIL-101(Cr)	800.42	719.87	0.513	2.56

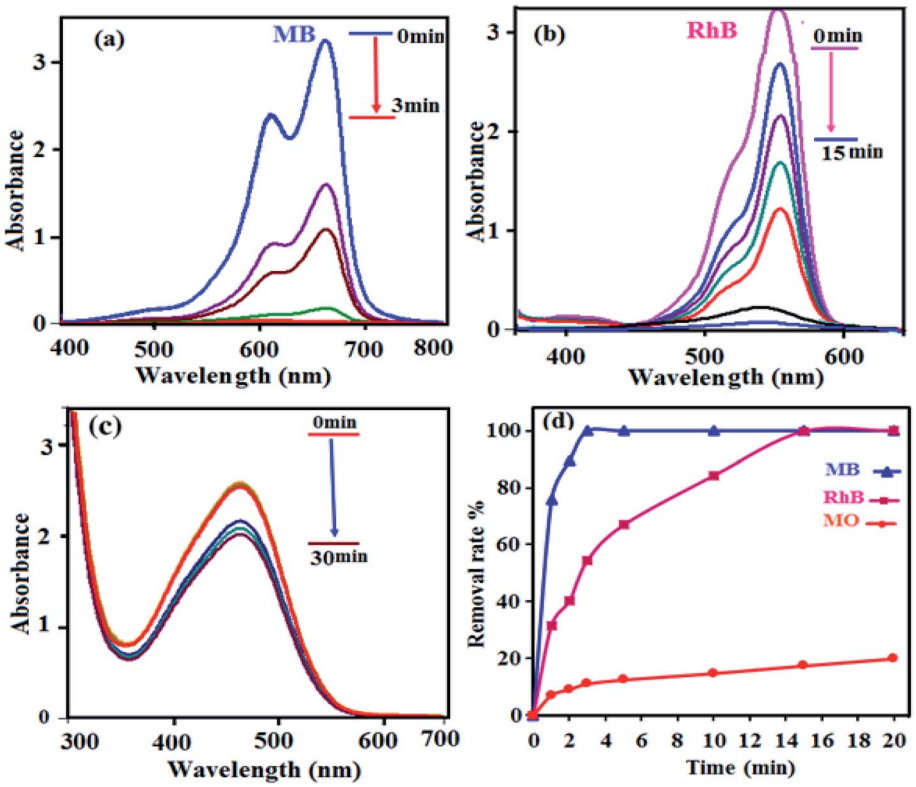

Fig. 7 The UV-Vis spectra during adsorption of dyes over P_2Mo_{18}/MIL-101(Cr): (a) MB, (b) RhB and (c) MO. (d) Comparison of the adsorption efficiencies of the dyes. Experimental conditions: $C_{0(MB)} = C_{0(RhB)} = C_{0(MO)} = 50$ mg L^{-1}, solution volume = 50 mL, adsorbent dosage = 30 mg, temperature = 25 °C and natural pH ≈ 6.5.

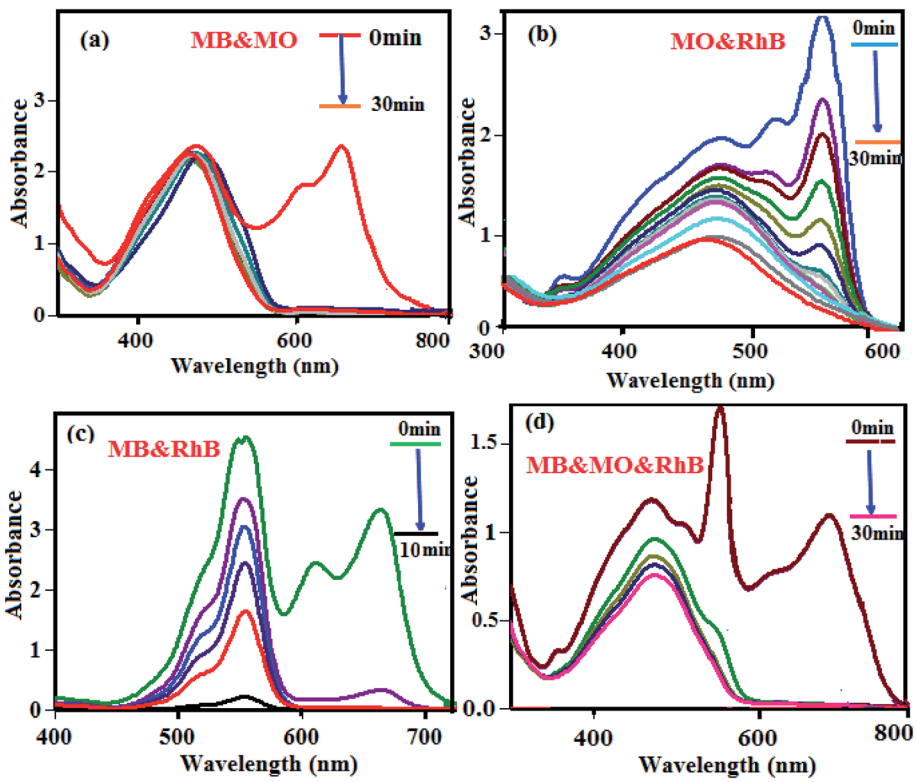

Fig. 8 The selective adsorption capacity of the P_2Mo_{18}/MIL-101(Cr) toward the mixed dyes of (a) MB + MO, (b) RhB + MO, (c) MB + RhB, and (d) MB + MO + RhB. Experimental conditions: $C_{0(MB)} = C_{0(RhB)} = C_{0(MO)} = 50$ mg L^{-1}, solution volume = 50 mL, adsorbent dosage = 30 mg, temperature = 25 °C and natural pH ≈ 6.5.

Table 2 Comparison of the adsorption capacities of various adsorbents for MB

Adsorbent	Adsorption capacity (mg g^{-1})	C_{MB} (mg L^{-1})	Time	Ref.
$\{Zn_3(PCAP)_2[CrMo_6(OH)_5O_{19}](H_2O)_6\}\cdot 6H_2O$	18.83	10	30 min	39
$H_6P_2W_{18}O_{62}$/MOF-5	51.81	10	10 min	47
MIL-68(Al)@SBA-15	62.93	25	0.5 min	48
PV_2Mo_{10}/M (membrane)	82	20	48 h	49
MOF-Cu-BTC	15.28	3.19	6 h	50
LnCu–POMs	391	20	1 min	51
$H_3PW_{12}O_{40}$/MIL-101(Fe)	473.7	100	5 min	52
P_5W_{30}/MIL-101(Cr)	212	200	8 min	53
CuS@PANI/PW_{12}	83.3	25	20 min	54
Fe_3O_4@AMCA-MIL53(Al)	325	25	240 min	55
Activated lignin–chitosan	34.70	82	200 min	56
P_2Mo_{18}/MIL-101(Cr)	312	200	30 min	This work

removal efficiency increases with increasing pH value from 2 to 10. At low pH, while the less negative surface of P_2Mo_{18}/MIL-101(Cr) does not favor the adsorption process as a result of the electrostatic repulsion, a substantial amount of dye adsorption onto P_2Mo_{18}/MIL-101(Cr) still takes place at low pH values, suggesting that π–π stacking interactions and/or hydrophobic interactions occur between MB and P_2Mo_{18}/MIL-101(Cr).[47] At high pH values, the presence of high concentrations of OH^- ions increases the negative charge on the P_2Mo_{18}/MIL-101(Cr) surface by deprotonating the positively charged sites. The negative charge value was sharply enhanced when the initial solution pH was increased from 2 to 10. At pH values ≥ 6, the surface of the adsorbent is negatively charged, which favors electrostatic interaction of cationic species of dye with the negatively charged surface. The electrostatic attraction force of MB with P_2Mo_{18}/MIL-101(Cr) is likely to be greater at greater pH values.[57,58]

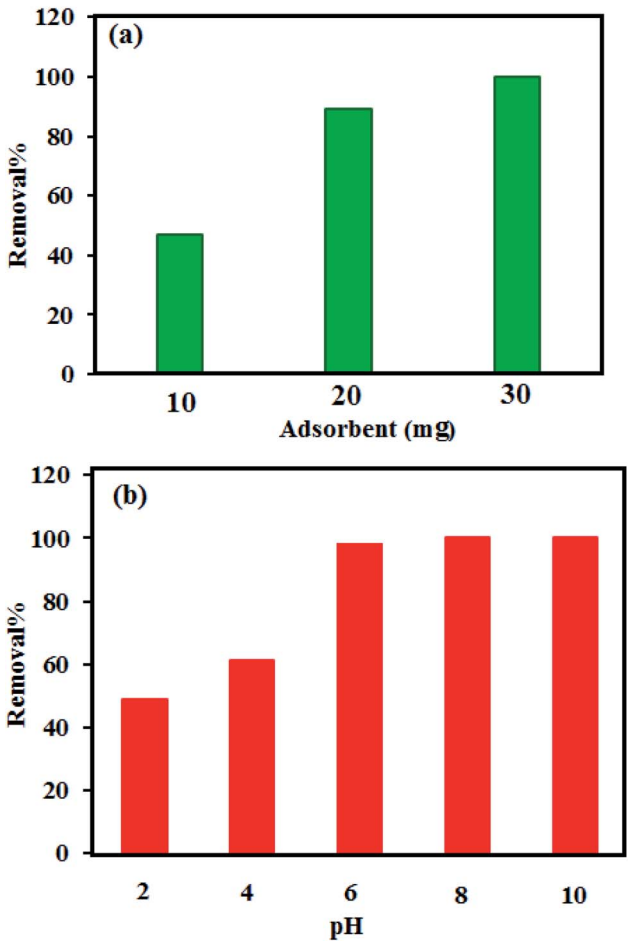

Fig. 9 (a) Effects of P_2Mo_{18}/MIL-101(Cr) dosage and (b) effects of initial pH on the removal efficiency of MB. Experimental conditions: $C_{0(MB)}$ = 50 mg L^{-1}, solution volume = 50 mL and temperature = 25 °C at a fixed adsorption time of 3 min.

3.7.4. Adsorption kinetics and adsorption isotherm. To adsorb dyes onto P_2Mo_{18}/MIL-101(Cr) at different dye concentration amounts (50, 80, 100, 120, 150, 170 and 200 mg L^{-1}), linear plots of t/q_t *versus* t are indicated in Fig. 10. As shown in Fig. 10(a), the quantity of MB adsorbed onto P_2Mo_{18}/MIL-101(Cr) increased swiftly with increasing adsorption time for the first 3 min, then slowed and finally reached an equilibrium point after about 20 min. It can be seen that the MB adsorption capacity of the P_2Mo_{18}/MIL-101(Cr) at equilibrium was enhanced from 100 to 312.5 mg g^{-1} by increasing the initial dye concentration from 50 to 200 mg L^{-1}.

In order to investigate the detailed characteristics of the adsorption behavior of P_2Mo_{18}/MIL-101(Cr), a pseudo-second-order kinetics model was applied. The pseudo-second-order kinetic equation is expressed as follows:[59]

$$t/q_t = 1/k_2q_e^2 + t/q \quad (3)$$

where k_2 is the rate constant of the pseudo-second-order model (g mg^{-1} min^{-1}), and q_e and q_t (mg g^{-1}) are the amounts of the dye adsorbed at equilibrium and at various times t (min), respectively. The values of q_e (cal) and k_2 were estimated from the slope and intercept of the linear isotherm of t/q_t *vs.* t, as shown in Fig. 10(b). The results are summarized in Table 3. Evidently, the correlation coefficients (R_2) are above 0.999, showing that the adsorption process can be fitted to the pseudo-second-order model. Furthermore, the values of q_e (exp) (mg g^{-1}) are lower than the calculated q_e (cal) (mg g^{-1}) according to

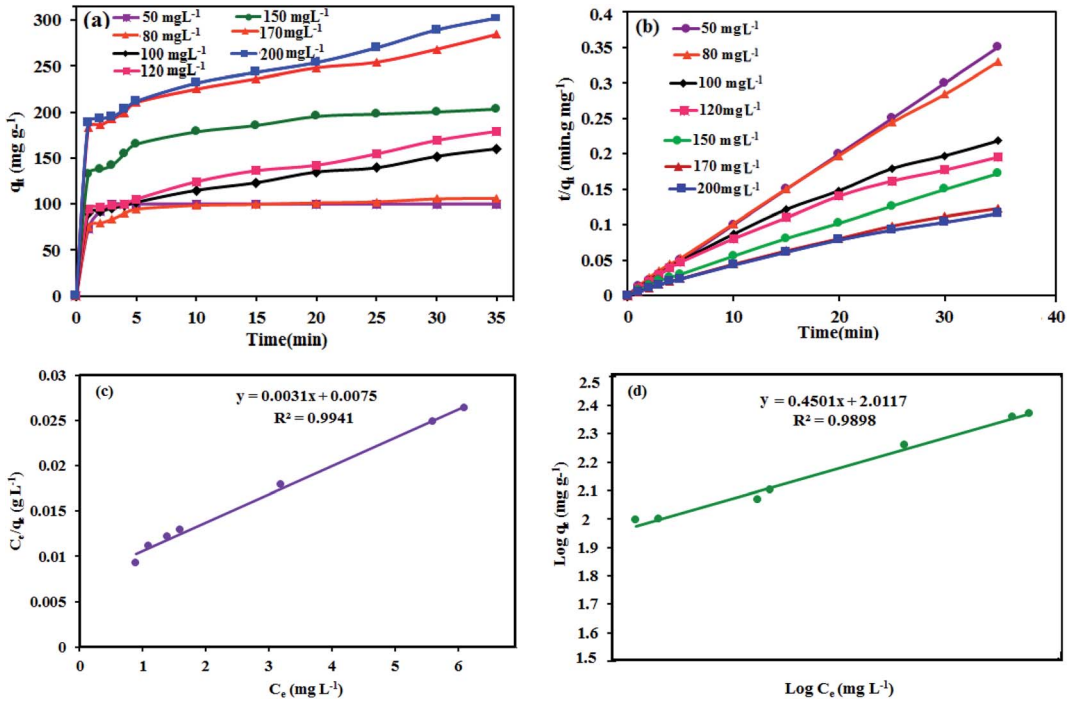

Fig. 10 (a) The effect of the initial dye concentration, (b) pseudo-second-order kinetics, (c) Langmuir and (d) Freundlich isotherms for the adsorption of MB onto the P_2Mo_{18}/MIL-101(Cr) nanocomposite. Experimental conditions: solution volume = 50 mL, adsorbent dosage = 30 mg and temperature = 25 °C.

Table 3 Adsorption kinetic parameters for the adsorption of MB onto P_2Mo_{18}/MIL-101(Cr)

Initial concentration of MB (mg L^{-1})	Pseudo-second-order kinetics			
	$q_{e,exp}$ (mg g^{-1})	k_2 (g mg^{-1} min^{-1})	$q_{e,cal}$ (mg g^{-1})	R^2
50	100	11.1	100	0.999
80	102	1.52	106.38	0.999
100	140	0.47	158.73	0.984
120	154	0.39	178.5	0.972
150	200	0.96	208	0.998
170	269	0.72	277.1	0.992
200	272	0.6	294	0.989

the pseudo-second-order equation. All of these results prove that the adsorption capacity can be correlated with the variation of the surface area and porosity of the adsorbent. As evidenced, a greater surface area and pore volume will afford a higher adsorption capacity.

Isotherm models of adsorption available in the literature, such as the Langmuir[60,61] and Freundlich[62,63] models, were engaged to explore the relationship between the amount of adsorbed dye (q_e) and the concentration of dye in the solution (C_e) when both are at equilibrium. The Langmuir equation can be expressed as eqn (4):

$$C_e/q_e = 1/k_L q_m + C_e/q_m \quad (4)$$

where C_e (mg L^{-1}) is the MB concentration at equilibrium, k_L is the Langmuir adsorption constant, q_e is the amount of dye adsorbed per gram of adsorbent (mg g^{-1}) at equilibrium concentration and q_m (mg g^{-1}) is the high adsorption capacity. The Langmuir isotherm displays that the amount of dye adsorbed grows as the concentration increases to a saturation point. As long as adsorption sites exist, the adsorption will increase with growing dye concentration; however, after the sites are occupied, any further increase in the concentration of dye will not lead to an increased amount of dye on the adsorbent (Fig. 10(c)). The dimensionless separation factor, R_L, is a critical characteristic of the Langmuir isotherm to describe the favorability of adsorption on an adsorbent, which is defined by the following eqn (5):[64]

$$R_L = 1/(1 + K_L C_0) \quad (5)$$

where C_0 (mg L^{-1}) is the initial concentration of the adsorbate MB. The value of R_L indicates that the isotherm is irreversible ($R_L = 0$), favorable ($0 < R_L < 1$), linear ($R_L = 1$) or unfavorable ($R_L > 1$ or $R_L < 0$). In the present study, the calculated value of R_L for the initial concentrations of MB was 0.014, which illustrates that the process of MB adsorption onto the P_2Mo_{18}/MIL-101(Cr) nanohybrid was favorable. The Freundlich isotherm exhibits multilayer adsorption onto the heterogeneous surface of the adsorbent based on the linear equation displayed below:

$$\log q_e = 1/n \log C_e + \log K_F \quad (6)$$

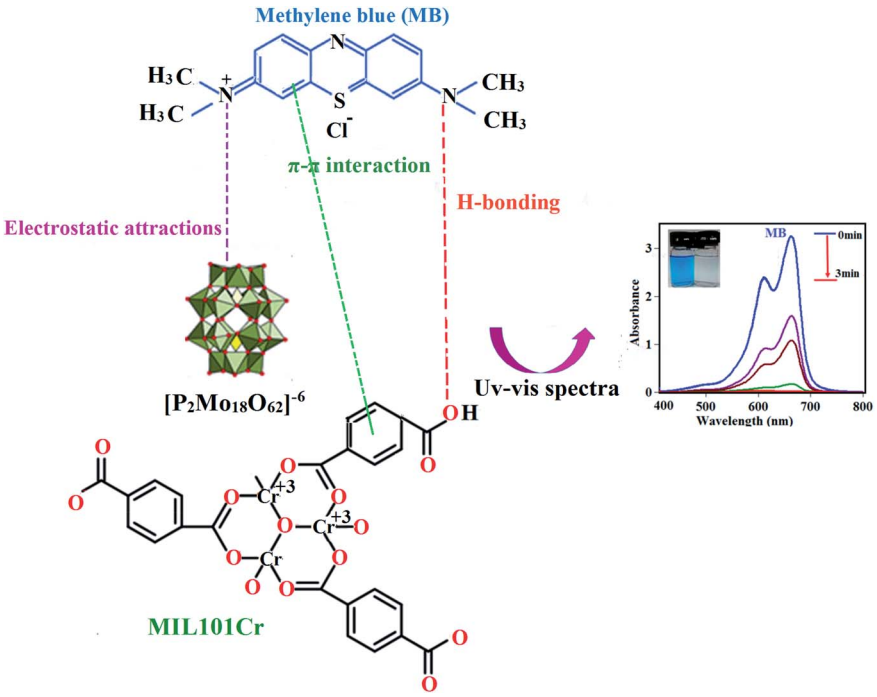

Fig. 11 Proposed mechanism for the adsorption of cationic MB dye using the P_2Mo_{18}/MIL-101(Cr) nanohybrid.

where K_F (L g^{-1}) and $1/n$ are the Freundlich characteristic constants, which show the adsorption capacity and intensity, respectively. The intercept and slope of a linear plot of ln q_e *versus* ln C_e give the values of K_F and $1/n$. The slope and intercept of the linear plot of log q_e *versus* log C_e can be used to estimate the values of $1/n$ and K_F (Fig. 10(d)). The values of R_2 in Table 3 are better fitted to the Langmuir model than to the Freundlich model.

3.7.5. Adsorption mechanism. The mechanism of adsorption of dye molecules by an adsorbent in aqueous solution can be affected by various influences, such as the surface properties of the composite, its textural properties, and the types of interactions occurring between the adsorbent and the dye molecules, such as hydrogen bonding, electrostatic attractions, π–π stacking and ion exchange. The adsorption sites play an important role in enhancing the adsorption capacity. Even though extra comprehensive effort is indispensable to clearly realize the mechanism of dye adsorption on P_2Mo_{18}/MIL-101(Cr), it can be simply clarified in terms of electrostatic interactions between MB and the adsorbent. The adsorption efficiency of the MIL-101(Cr) sample, despite its higher surface area, was lower than that of the P_2Mo_{18}/MIL-101(Cr) nanohybrid (see Table 1). This confirms that other factors influence the adsorption efficiency in addition to the specific surface area of the adsorbent. After introducing the P_2Mo_{18} polyanions into the cavities of MIL-101(Cr), it was confirmed that the adsorption capacity of the nanocomposite changed greatly compared with that of MIL-101(Cr). This is because of the rapid and effective adsorption of cationic MB and RhB dyes by P_2Mo_{18} polyanions, whereas it is unfavorable for P_2Mo_{18}/MIL-101(Cr) to adsorb the anionic dye MO, as shown in Fig. 7 and 8. The attained outcomes for the selective adsorption of cationic dyes in the presence of anionic MO dye undoubtedly suggest that the adsorption of MB dye on the P_2Mo_{18}/MIL-101(Cr) nanocomposite is linked to the electrostatic interaction between the cationic dye molecules and the P_2Mo_{18} polyanions with high negative charge (6^-). These findings indicate that the P_2Mo_{18} polyoxoanion clusters encapsulated in the mesoporous cages of MIL-101(Cr) act as the active sites for the adsorption of cationic dye molecules.

The zeta potential of a material is another key factor influencing its adsorption capacity; therefore, this was tested to understand further why the P_2Mo_{18}/MIL-101(Cr) sample can remove the cationic dyes MB and RhB more effectively than the anionic MO dye. As shown in Fig. S1,† the zeta potentials of the MIL-101(Cr) and P_2Mo_{18}/MIL-101(Cr) samples were measured as +16.75 and −24.02 mV, respectively, in water at natural pH. This finding illustrates that the higher efficiency of the removal of cationic dyes can be mainly attributed to the electrostatic attraction interactions between the adsorbent and the cationic dye. After modification with P_2Mo_{18}, the obtained P_2Mo_{18}/MIL-101(Cr) showed a more negative zeta potential than pristine MIL-101(Cr); thus, it is capable of adsorbing more of the cationic dyes MB and RhB, whereas it is unfavorable for P_2Mo_{18}/MIL-101(Cr) to adsorb the anionic dye MO. The simplified mechanism of MB adsorption is illustrated in Fig. 11.

3.8. Stability and recyclability

The adsorption of MB onto the P_2Mo_{18}/MIL-101(Cr) nanohybrid was confirmed using various techniques. Fig. S2† shows the FT-IR spectra of MB dye and the P_2Mo_{18}/MIL-101(Cr) nanohybrid before and after the adsorption of MB dye (abbreviated

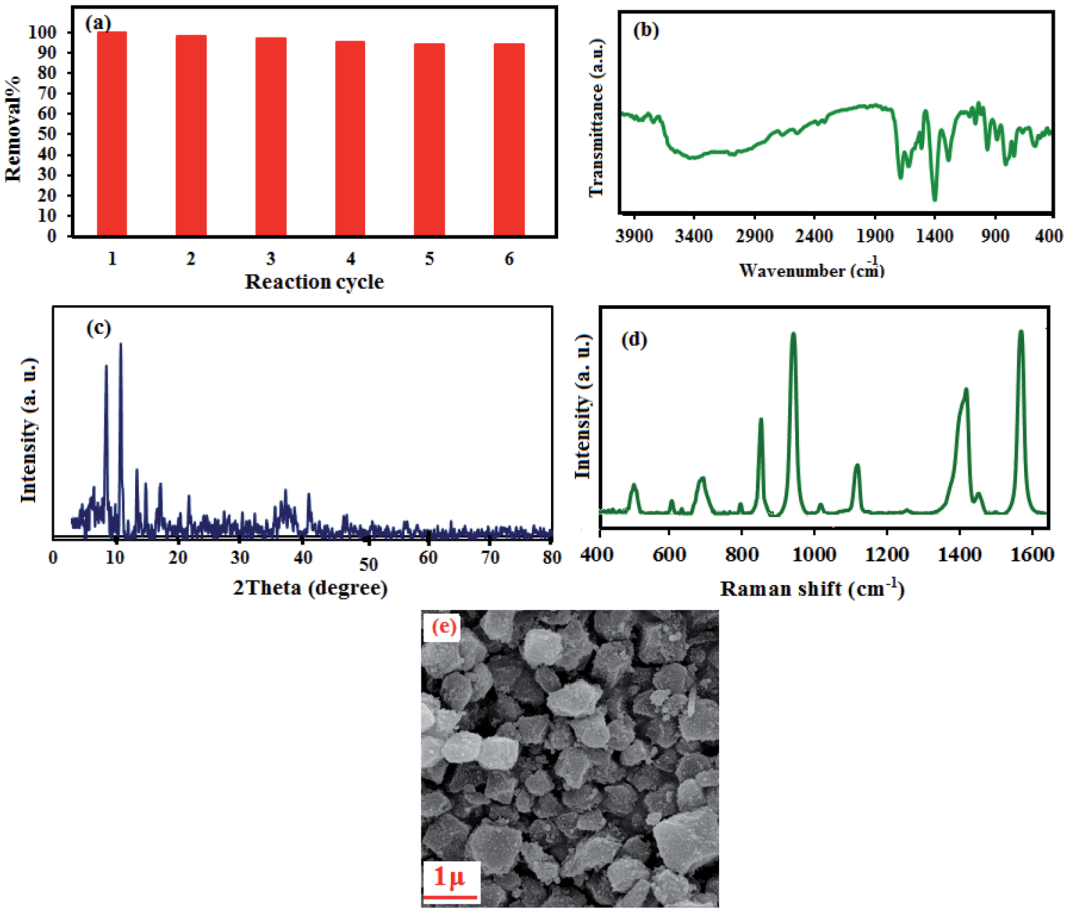

Fig. 12 (a) Recyclability of the P_2Mo_{18}/MIL-101(Cr) nanocomposite, (b) FT-IR, (c) XRD, (d) FT-Raman and (e) SEM images of the recovered P_2Mo_{18}/MIL-101(Cr) nanohybrid after the sixth run.

as MB@P_2Mo_{18}/MIL-101(Cr)). The presence of the characteristic peaks of MB molecule at 1598 cm^{-1} (C=C aromatic), 1390 cm^{-1} (C=N aromatic) and 1334 cm^{-1} (C–N) confirmed the adsorption of MB dye into the P_2Mo_{18}/MIL-101(Cr) hybrid. Furthermore, these bands were not seen in the spectrum of the P_2Mo_{18}/MIL-101(Cr) nanohybrid. In addition, the EDX spectrum and elemental mappings of MB@P_2Mo_{18}/MIL-101(Cr) in Fig. S3 and S4† revealed the existence of N, Cl and S elements and their homogeneous distributions in the adsorbent. This finding further indicates that the MB molecules were successfully adsorbed on the surface of the P_2Mo_{18}/MIL-101(Cr) nanohybrid. Micrographs of MB@P_2Mo_{18}/MIL-101(Cr) are shown in Fig. S5.† It can be observed that the recovered adsorbent almost retained its initial size and morphology. As shown in Fig. S6,† the XRD pattern of MB@P_2Mo_{18}/MIL-101(Cr) showed no change in comparison with the pattern of the fresh nanohybrid in Fig. 3(c). The N_2 gas adsorption–desorption isotherms and pore size distributions of MB@P_2Mo_{18}/MIL-101(Cr) are shown in Fig. S7a and b.† Compared with P_2Mo_{18}/MIL-101(Cr) (see Fig. 6 and Table 1), MB@P_2Mo_{18}/MIL-101(Cr) demonstrated a significant decrease in both pore volume (from 0.513 to 0.018 $cm^3\ g^{-1}$) and surface area (800.42 to 182.18 $m^2\ g^{-1}$), confirming the insertion of large MB molecules into the pores of P_2Mo_{18}/MIL-101(Cr) and occupation of the main part of the pore space.

The reusability of an adsorbent is a vital aspect of its practical application based on economic considerations in wastewater treatment efficiency. This nanohybrid was effortlessly separated after the adsorption process by simple centrifugation due to its insolubility in water. The adsorbed MB was removed from P_2Mo_{18}/MIL-101 by washing several times with 1 : 1 water and ethanol solution; then, the P_2Mo_{18}/MIL-101 was reused for a new adsorption experiment. The recycling adsorption efficiency was disclosed in Fig. 12(a). An adsorption efficiency of 94% was achieved after six cycles. The nature of the recovered nanohybrid after desorbing MB dye was also tested. As shown in Fig. 12(b–e), the FT-IR, XRD, FT-Raman and SEM analyses of the recovered P_2Mo_{18}/MIL-101(Cr) adsorbent did not show significant changes in comparison with the fresh adsorbent. The above results further confirmed that the adsorption process did not affect the structure and properties of the adsorbent. At the end, these findings confirm that the adsorbent can effectively remove cationic dyes from aqueous solution with reusability and high separation efficiency.

4. Conclusions

P_2Mo_{18}/MIL-101(Cr) nanocomposites with a high BET specific surface area of 800.42 m^2 g^{-1} were successfully prepared by a simple one-pot hydrothermal procedure. The results obtained from XRD, FT-IR, FT-Raman, FE-SEM, and EDS techniques confirmed the successful incorporation of the P_2Mo_{18} in the MIL-101(Cr) framework. The results revealed that the adsorption process followed a pseudo-second-order kinetic model as well as the Langmuir isotherm model. Also, the hybrid nanomaterial could easily be separated from aqueous solution after adsorption experiments and recycled several times without any loss in its adsorption ability. Therefore, P_2Mo_{18}/MIL-101(Cr) can be applied as a promising adsorbent for the treatment of dye effluents.

Conflicts of interest

There are no conflicts of interest to declare.

Acknowledgements

The authors gratefully acknowledge the Lorestan University Research Council for the financial support.

References

1 F. Siadatnasab, S. Farhadi, M. Dusek, V. Eigner, A.-A. Hoseini and A. Khataee, *Ultrason. Sonochem.*, 2019, **64**, 104727.
2 V. Katheresan, J. Kansedo and S. Y. Lau, *J. Environ. Chem. Eng.*, 2018, **6**, 4676–4697.
3 A.-A. Hoseini, S. Farhadi, A. Zabardasti and F. Siadatnasab, *RSC Adv.*, 2019, **9**, 24489–24504.
4 S. Farhadi, F. Siadatnasab and A. Khataee, *Ultrason. Sonochem.*, 2017, **37**, 298–309.
5 A. Hamedi, M. B. Zarandi and M. R. Nateghi, *J. Environ. Chem. Eng.*, 2019, **7**, 102882.
6 S. Farhadi and F. Siadatnasab, *J. Mol. Struct.*, 2016, **1123**, 171–179.
7 Y. Wang, L. Zhu, X. Wang, W. Zheng, C. Hao, C. Jiang and J. Wu, *J. Ind. Eng. Chem.*, 2018, **61**, 321–330.
8 J. M. Lim, J. Park, J. T. Park and S. Bae, *J. Ind. Eng. Chem.*, 2019, **71**, 378–386.
9 C. H. Nguyen and R.-S. Juang, *J. Ind. Eng. Chem.*, 2019, **76**, 296–309.
10 S. Farhadi and F. Siadatnasab, *Mater. Res. Bull.*, 2016, **83**, 345–353.
11 M. Naushad, G. Sharma and Z. A. Alothman, *J. Clean. Prod.*, 2019, **241**, 118263.
12 M. Naushad, A. A. Alqadami, Z. A. Alothman, I. H. Alsohaimi, M. S. Algamdi and A. M. Aldawsari, *J. Mol. Liq.*, 2019, **293**, 111442.
13 N. S. Shah, J. A. Khan, M. Sayed, Z. U. H. Khan, J. Iqbal, S. Arshad, M. Junaid and H. M. Khan, *Sep. Purif. Technol.*, 2020, **233**, 115966.
14 S. Guo, K. Wu, Y. Gao, L. Liu, X. Zhu, X. Li and F. Zhang, *J. Chem. Eng. Data*, 2018, **63**, 3902–3912.
15 J. Shu, R. Liu, H. Wu, Z. Liu, X. Sun and C. Tao, *J. Taiwan Inst. Chem. Eng.*, 2018, **82**, 351–359.
16 S. Farhadi and F. Siadatnasab, *Desalin. Water Treat.*, 2017, **66**, 299–308.
17 J. C. Ye, J. J. Chen, R. M. Yuan, D. R. Deng, M. S. Zheng, L. Cronin and Q. F. Dong, *J. Am. Chem. Soc.*, 2018, **140**, 3134–3138.
18 R.-Z. Zhang, S. Quan, M. Xia, Q. Wang, W. Zhang and J.-M. Yang, *J. Colloid Interface Sci.*, 2018, **525**, 54–61.
19 J.-M. Yang, R.-J. Ying, C.-X. Han, Q.-T. Hu, H.-M. Xu, J.-H. Li, Q. Wang and W. Zhang, *Dalton Trans.*, 2018, **47**, 3913–3920.
20 A. Hayashi, M. N. K. Wihadi, H. Ota, X. López, K. Ichihashi, S. Nishihara, K. Inoue, N. Tsunoji, T. Sano and M. Sadakane, *ACS omega*, 2018, **3**, 2363–2373.
21 J. Zhang, J. Luo, P. Wang, B. Ding, Y. Huang, Z. Zhao, J. Zhang and Y. Wei, *Inorg. Chem.*, 2015, **54**, 2551–2559.
22 S. Farhadi, M. Dusek, F. Siadatnasab and V. Eigner, *Polyhedron*, 2017, **126**, 227–238.
23 Y.-R. Chen, K.-H. Liou, D.-Y. Kang, J.-J. Chen and L.-C. Lin, *Langmuir*, 2018, **34**, 4180–4187.
24 Y.-Z. Chen, R. Zhang, L. Jiao and H.-L. Jiang, *Coord. Chem. Rev.*, 2018, **362**, 1–23.
25 P. D. Du, H. T. M. Thanh, T. C. To, H. S. Thang, M. X. Tinh, T. N. Tuyen, T. T. Hoa and D. Q. Khieu, *J. Nanomater.*, 2019, 2019.
26 C. Chen, L. Wang, B. Zhu, Z. Zhou, S. I. El-Hout, J. Yang and J. Zhang, *J. Energy Chem.*, 2020, **54**, 528–554.
27 Y.-T. Liao, B. M. Matsagar and K. C.-W. Wu, *ACS Sustain. Chem. Eng.*, 2018, **6**, 13628–13643.
28 H. Konnerth, B. M. Matsagar, S. S. Chen, M. H. Prechtl, F.-K. Shieh and K. C.-W. Wu, *Coord. Chem. Rev.*, 2020, **416**, 213319.
29 C.-C. Chueh, C.-I. Chen, Y.-A. Su, H. Konnerth, Y.-J. Gu, C.-W. Kung and K. C.-W. Wu, *J. Mater. Chem.*, 2019, **7**, 17079–17095.
30 C. C. Lee, C. I. Chen, Y. T. Liao, K. C. W. Wu and C. C. Chueh, *Adv. Sci.*, 2019, **6**, 1970030.
31 Y. V. Kaneti, S. Dutta, M. S. Hossain, M. J. Shiddiky, K. L. Tung, F. K. Shieh, C. K. Tsung, K. C. W. Wu and Y. Yamauchi, *Adv. Mater.*, 2017, **29**, 1700213.
32 G. Gumilar, Y. V. Kaneti, J. Henzie, S. Chatterjee, J. Na, B. Yuliarto, N. Nugraha, A. Patah, A. Bhaumik and Y. Yamauchi, *Chem. Sci.*, 2020, **11**, 3644–3655.
33 C. Gecgel, U. B. Simsek, B. Gozmen and M. Turabik, *J. Iran. Chem. Soc.*, 2019, **16**, 1735–1748.
34 Q. Wu, M. Niu, X. Chen, L. Tan, C. Fu, X. Ren, J. Ren, L. Li, K. Xu and H. Zhong, *Biomaterials*, 2018, **162**, 132–143.
35 Y. Zhang, F. Wang, C. Liu, Z. Wang, L. Kang, Y. Huang, K. Dong, J. Ren and X. Qu, *ACS Nano*, 2018, **12**, 651–661.
36 J. Kou and L.-B. Sun, *ACS Appl. Mater. Interfaces*, 2018, **10**, 12051–12059.
37 E. Arendt, S. Zehri, P. Eloy and E. M. Gaigneaux, *Eur. J. Inorg. Chem.*, 2012, **2012**, 2792–2801.
38 B. Hong, L. Liu, S.-M. Wang and Z.-B. Han, *J. Clust. Sci.*, 2016, **27**, 563–571.
39 G. Marci, E. I. Garcia-Lopez, F. R. Pomilla, L. F. Liotta and L. Palmisano, *Appl. Catal. A: Gen.*, 2016, **528**, 113–122.

40 F. Jing, R. Liang, J. Xiong, R. Chen, S. Zhang, Y. Li and L. Wu, *Appl. Catal. B: Environ.*, 2017, **206**, 9–15.
41 J.-H. Li, X.-L. Wang, G. Song, H.-Y. Lin, X. Wang and G.-C. Liu, *Dalton Trans.*, 2020, **49**, 1265–1275.
42 Z. M. Zhang, S. Yao, Y. G. Li, X. B. Han, Z. M. Su, Z. S. Wang and E. B. Wang, *Chem.–Eur. J.*, 2012, **18**, 9184–9188.
43 L. M. Martínez Tejada, A. Muñoz, M. Centeno and J. A. Odriozola, *J. Raman Spectrosc.*, 2016, **47**, 189–197.
44 H. Chen, S. Chen, X. Yuan and Y. Zhang, *Mater. Lett.*, 2013, **100**, 230–232.
45 X.-J. Dui, W.-B. Yang, X.-Y. Wu, X. Kuang, J.-Z. Liao, R. Yu and C.-Z. Lu, *Dalton Trans.*, 2015, **44**, 9496–9505.
46 E. Amdeha and R. S. Mohamed, *Environ. Technol.*, 2019, 1–18.
47 X. Liu, W. Gong, J. Luo, C. Zou, Y. Yang and S. Yang, *Appl. Surf. Sci.*, 2016, **362**, 517–524.
48 F. Mahmoudi and M. M. Amini, *J. Water Process. Eng.*, 2020, **35**, 101227.
49 L. Yao, L. Zhang, R. Wang, S. Chou and Z. Dong, *J. Hazard.Mater.*, 2016, **301**, 462–470.
50 S. Lin, Z. Song, G. Che, A. Ren, P. Li, C. Liu and J. Zhang, *Micropor. Mesopor. Mater.*, 2014, **193**, 27–34.
51 F.-Y. Yi, W. Zhu, S. Dang, J.-P. Li, D. Wu, Y.-h. Li and Z.-M. Sun, *Chem. Commun.*, 2015, **51**, 3336–3339.
52 T.-T. Zhu, Z.-M. Zhang, W.-L. Chen, Z.-J. Liu and E.-B. Wang, *RSC Adv.*, 2016, **6**, 81622–81630.
53 A. A. Hoseini, S. Farhadi and A. Zabardasti, *Appl. Organomet. Chem.*, 2019, **33**, e4656.
54 F. Siadatnasab, K. Karami and A. Khataee, *J. Ind. Eng. Chem.*, 2019, **80**, 205–216.
55 A. A. Alqadami, M. Naushad, Z. Alothman and T. Ahamad, *J. Environ. Manag.*, 2018, **223**, 29–36.
56 A. B. Albadarin, M. N. Collins, M. Naushad, S. Shirazian, G. Walker and C. Mangwandi, *Chem. Eng. J.*, 2017, **307**, 264–272.
57 Y. Shao, L. Zhou, C. Bao, J. Ma, M. Liu and F. Wang, *Chem. Eng.*, 2016, **283**, 1127–1136.
58 T. Wang, P. Zhao, N. Lu, H. Chen, C. Zhang and X. Hou, *Chem. Eng.*, 2016, **295**, 403–413.
59 V. V. Kumar, S. Sivanesan and H. Cabana, *Sci. Total Environ.*, 2014, **487**, 830–839.
60 Z. Jiang and Y. Li, *Taiwan Inst. Chem. Eng.*, 2016, **59**, 373–379.
61 S. Aslam, J. Zeng, F. Subhan, M. Li, F. Lyu, Y. Li and Z. Yan, *J. Colloid Interface Sci.*, 2017, **505**, 186–195.
62 S. Ahmadi, L. Mohammadi, A. Rahdar, S. Rahdar, R. Dehghani, C. A. Igwegbe and G. Z. Kyzas, *Nanomaterials*, 2020, **10**, 556.
63 D. P. Dutta and S. Nath, *J. Mol. Liq.*, 2018, **269**, 140–151.
64 C. Jiao, Y. Wang, M. Li, Q. Wu, C. Wang and Z. Wang, *J. Magn. Magn. Mater.*, 2016, **407**, 24–30.